coatings

Communication

Buckling Characteristics of Different Cross-Sectioned LGFR-PP Stiffeners under Axial Compression

Jin Nie [1,2,*], Wenbo Gao [3] and Guibing Li [3]

[1] Loudi Vocational and Technical College, Loudi 417000, China
[2] State Key Laboratory of Advanced Design and Manufacturing for Vehicle Body, Hunan University, Changsha 410082, China
[3] School of Mechanical Engineering, Hunan University of Science and Technology, Xiangtan 411201, China
* Correspondence: nie0822@hnu.edu.cn

Abstract: Long glass fiber-reinforced polypropylene (LGFR-PP) composite structures with stiffeners are important substitutes for metal parts for vehicle lightweighting; a good understanding of the buckling characteristics of LGFR-PP stiffeners would provide an important reference for engineering design. The current work is therefore intended to study the buckling characteristics of different cross-sectioned LGFR-PP stiffeners under axial compression via experimental and theoretical analysis. Firstly, LGFR-PP stiffeners with semicircular, rectangular, and trapeziform cross-sections were compressed at the axial direction using a universal testing machine to obtain the buckling process data. Then, the elasticity stability theory modified according to the experimental results was derived to estimate the buckling resistance of LGFR-PP stiffeners in different designs. The test results showed that the LGFR-PP stiffeners possessed a flexible–torsional bulking instability mode under axial compression, the LGFR-PP stiffeners with a semicircular cross-section had higher compression buckling resistance, and the rectangular and trapeziform cross-sectioned stiffeners had better rigidity. The theoretical analysis showed that the modified elasticity stability theory could generally predict the buckling resistance of LGFR-PP stiffeners under axial compression.

Keywords: LGFR-PP; stiffeners; buckling characteristics; cross-section

Citation: Nie, J.; Gao, W.; Li, G. Buckling Characteristics of Different Cross-Sectioned LGFR-PP Stiffeners under Axial Compression. *Coatings* **2023**, *13*, 763. https://doi.org/10.3390/coatings13040763

Academic Editor: Roberto Montanari

Received: 6 March 2023
Revised: 28 March 2023
Accepted: 4 April 2023
Published: 12 April 2023

1. Introduction

Glass fiber-reinforced thermoplastic composites are increasingly applied in engineering design given their high strength/weight ratio, high recycling rate, low cost, and short manufacturing cycle [1–8]. Particularly in the automobile industry, glass fiber-reinforced thermoplastic composites are widely employed as substitutes for metal parts for lightweighting design [9,10], where the mechanical properties of stiffness, ultimate capacity, and failure mechanism structures are the main considerations in the design and application of composites.

In the past several decades, many studies have focused on improving the mechanical properties of structures through reinforced designs with a fiber-reinforced polymer (FRP) [11–20]. For example, Nassiraei and Rezadoost recently published a series of studies on the static capacity of tubular components in different connections (X-joints and T/Y-joints) reinforced with FRP, which provided an important reference for engineering design [11–13]. On the other hand, a stiffener is one of the most frequently used approaches as it can increase the distortion resistance, structural stiffness, and energy-absorbing capability with some weight addition [14]. Some studies have attempted to improve the strength and energy-absorbing capability of a polymer composite or hybrid toughened kenaf/glass epoxy composite bumper beam with reinforced stiffeners (or named as ribs) [15,16]; the results from these studies showed that the reinforced stiffeners could obviously improve the stiffness, strength, and energy-absorbing performance [15,16]. Previous studies also indicate that the geometrical (e.g., cross-section geometry and thickness) and welding parameters (e.g., bottom fillet and weld line area and position) could affect the strength of stiffeners [17–19]. The authors of [20] investigated the effect of the design of reinforced stiffeners on the energy-absorbing capacity of high-density expanded polypropylene, and concluded that the energy absorption of high-density expanded polypropylene could be optimized by fine-tuning the thickness and height of the reinforced stiffeners. Marco and Giovanni investigated a prototype composite rib structure and the experimental result showed that reinforced stiffeners could significantly improve the specific stiffness and strength of the laminate [9]. Despite some investigations on stiffeners, most of the above studies focus on a single type of cross-section, with few studies on long glass fiber-reinforced polypropylene (LGFR-PP) structures.

LGFR-PP is used to manufacture load-carrying structures, where the stiffener concept can be applied in LGFR-PP components to lighten their weight [21]. In semi-structural and structural components, such as battery compartments, bumper beams, etc., open-channel thin-walled composites are widely used as they are prone to buckling under compressive loading [22]. Since the buckling resistance and stiffness of LGFR-PP components could be significantly enhanced by appropriately adding stiffeners, engineers need to select the most suitable cross-section shape and size of the LGFR-PP stiffener for semi-structural and structural components under a compressive load. Moreover, the corresponding theoretical analysis on the mechanical properties and instability mode of the stiffeners would provide an important reference for the selection of LGFR-PP stiffeners. Therefore, the current study focuses on experimental investigations and theoretical analyses of the instability mode and mechanical properties of LGFR-PP stiffeners subjected to axial compression; in particular, the influences of the cross-section geometry (semicircular, rectangular, and trapeziform) are considered.

2. Experimental Study

2.1. Experimental Setup

The LGFR-PP composite used in the current work was prepared by composing long E-glass fibers with a polypropylene matrix, where glass fibers of around 40 mm in length and 13 µm in diameter were employed, which were randomly oriented in the polymer matrix. In the LGFR-PP composite, the weight of glass fibers accounted for 40%; this was chosen since this glass mass fraction could offer a peak strength to LGFR-PP composites [21]. Then, LGFR-PP stiffeners with semicircular (Type I), rectangular (Type II), and trapeziform (Type III) cross-sections were prepared via the hot-molding method, which is widely used for LGFR-PP composite production [4,10].

The geometries of the different cross-sectioned stiffeners (Type I–III) are shown in Figure 1. The thickness t of specimens is 3 mm, L (the length of specimens) is from 145 mm to 220 mm, w represents the width (98 mm), and R represents the corner radius (2 mm). The arc length (l) from point A to B is 33 mm for the semicircular and trapeziform cross-sections and 17.27 mm for the specimens in the rectangular cross-section. Then, the different cross-sectioned specimens were compressed at the axial direction using a universal testing machine (E44, MTS Systems Co., Eden Prairie, MN, USA). The loading velocity for the compression test was set as 12 mm/min loaded on the ends of the specimens. In order to guarantee reliable experimental data, five compression tests were repeated for the same designed cross-section; in total, 45 samples (3 cross-section types*3 samples of different lengths for each cross-section type*5 repetitions for each design) were tested. Then, the peak force (F_{max}) and the displacement (S_{max}) at the instant of F_{max} were used as the evaluation index in investigating the mechanical properties of LGFR-PP stiffeners with different cross-sections or lengths under compression. Specifically, the greater F_{max} reflects the greater buckling resistance of the design, and the smaller S_{max} means better rigidity.

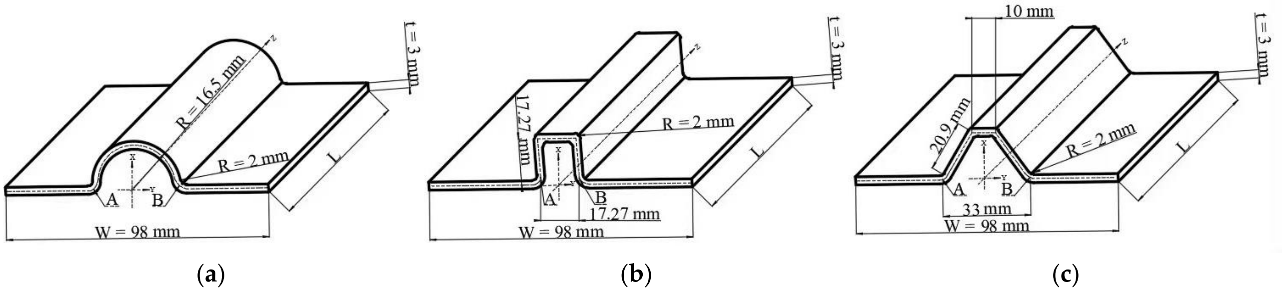

Figure 1. Geometries of the different cross-sectioned stiffeners: (**a**) Type I (semicircular), (**b**) Type II (rectangular), and (**c**) Type III (trapeziform).

2.2. Experimental Results

Figure 2 shows the average value and standard deviation of the F_{max} and S_{max} for each cross-section shape calculated from the experimental data. It is clear from the data that the F_{max} decreases when increasing the length of specimens (L), while the S_{max} increases with the enlargement of L; the specimens with the semicircular cross-section (Type I) have a higher average F_{max} and S_{max} than the specimens with the rectangular cross-section (Type II) and trapeziform cross-section (Type III) for a given L, and the average S_{max} for Type II specimens is similar to that of Type III when L is in the range of 145 mm to 185 mm. Figure 3 shows the typical deformation process, instability mode, failure behavior, and force–displacement relationship (simplified from the raw data) of the specimens under compression. It could be observed that the deformation was caused by a bending–torsion combined load, and the failure behavior includes matrix cracking, fiber pull-out, or fiber breakage. The force–displacement curve indicates that four typical phases (elastic–plastic–breakage–failure) could be distinguished, and the elastic–plastic deformation phase is dominant, while the breakage phase is relatively short.

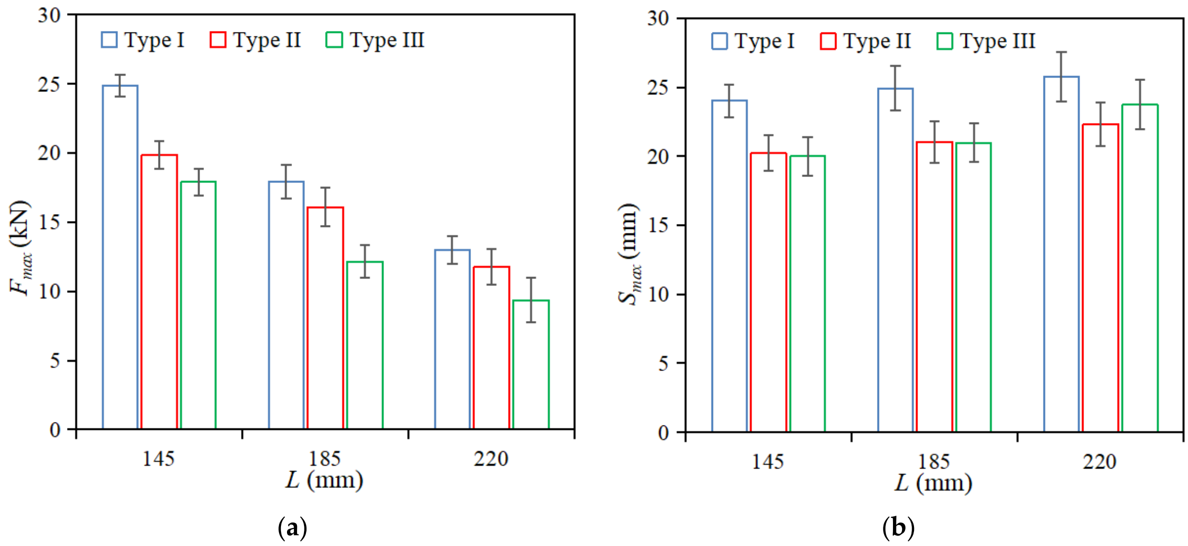

Figure 2. The average and standard deviation of F_{max} (**a**) and S_{max} (**b**) for the specimens with different cross-sections and lengths, calculated from the experimental data.

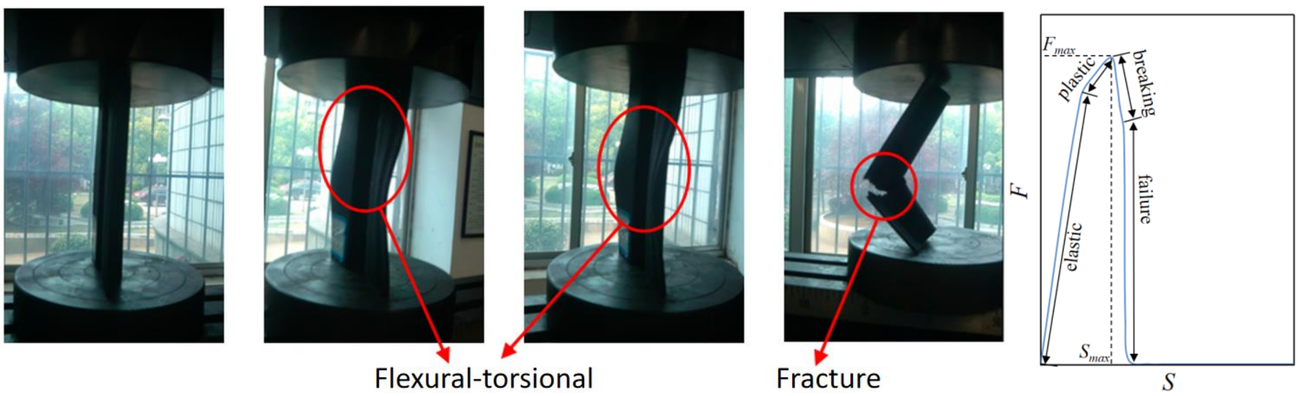

Figure 3. The typical deformation process, failure behavior, and force–displacement relationship of the specimens under compression (S: displacement, F: force, F_{max}: peak force, S_{max}: displacement at the instant of F_{max}).

3. Theoretical Study

In this section, the instability mode of LGFR-PP stiffeners subjected to axial compression is studied based on the elasticity stability theory for uniform cross-sectioned open thin-walled bars in metal materials. As shown in Figure 4, it is supposed that L is the length of a specimen, A is the area of the cross-section, O is the section centroid, x and y represent the principal inertia axes of the cross-section, and z is the centroidal axis. S represents the flexural center of the cross-section and the corresponding coordinate is (xc, yc). When the axial pressure P is increased to the critical value P_{cr}, the twisting or bending of the specimen may take place, which leads to a loss of stability for the specimen. Assume that the specimen is in a neutral equilibrium state, and its independent displacement components include the displacements u and v of the bending center S in the axes x and y direction and the torsion angle ϕ of the cross-section around the bending center. The u and v coinciding with the forward axis are positive. The sign of ϕ is determined by the right-hand screw rule. The u, v, and ϕ are functions of z.

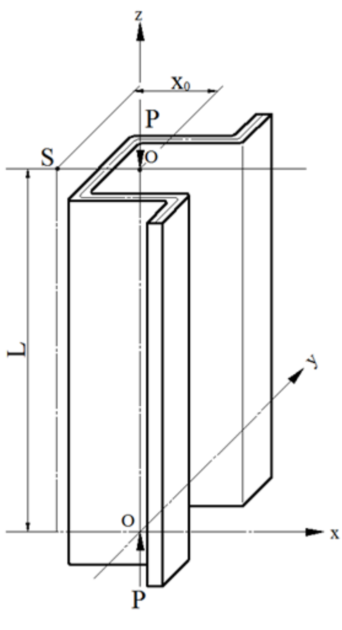

Figure 4. Geometrical and coordinate parameters of the uniform cross-sectioned open thin-walled bar (L: length, S: flexural center, P: pressure, O: section centroid, x and y: principal inertia axes, z: centroidal axis).

According to the experimental conditions, it is obtained that the specimens are hinged at both ends, and the cross-section of the end has freedom to warp [23,24]. When the boundary condition is $z = 0$ and $z = L$, $u = v = \phi = 0$, $\frac{d^2u}{dz^2} = \frac{d^2v}{dz^2} = \frac{d^2\phi}{dz^2} = 0$, and the deformation assumption that satisfies the boundary conditions can be obtained:

$$\begin{array}{l} u = \xi \sin\frac{n\pi z}{L} \\ v = \eta \sin\frac{n\pi z}{L} \quad (n = 1, 2, 3, L) \\ \phi = \psi \sin\frac{n\pi z}{L} \end{array} \tag{1}$$

where ξ, η, and ψ are undetermined parameters.

The total potential energy of the open thin-walled bar under axial compression can be expressed as

$$\Pi = \frac{1}{2}\int_0^l \left[\begin{array}{l} EI_y u''^2 + EI_x v''^2 + EI_\omega \phi''^2 + \\ (GI_t - Pi_0^2)\phi'^2 - P\left(u'^2 + v'^2\right) + 2Px_0 v'\phi' \end{array} \right] dz \tag{2}$$

where E represents the elastic modulus, G is the shear modulus, I_x and I_y are the inertia moments of the cross-section for the axis x, and I_t and I_ω represent the torsional moment of inertia and fan-shape moment of inertia for the cross-section, respectively.

$$i_0^2 = \frac{I_x + I_y}{A} + x_0^2 \tag{3}$$

where x_0 is the distance between the flexural center and centroid.

By substituting Equation (1) into Equation (2) and the integral, the total potential energy Π of the specimens tested in the current work can be calculated from Equation (4) using the parameter values shown in Table 1.

$$\Pi = \left(\frac{n\pi}{L}\right)^2 \cdot \frac{l}{4} \left\{ \begin{array}{l} \xi^2\left[\left(\frac{n\pi}{L}\right)^2 EI_y - P\right] + \eta^2\left[\left(\frac{n\pi}{L}\right)^2 EI_x - P\right] \\ +\psi^2\left[\left(\frac{n\pi}{L}\right)^2 EI_\omega + GI_t - Pi_0^2\right] + 2\eta\psi P x_0 \end{array} \right\} \tag{4}$$

Table 1. The parameter values for Equation (4).

Specimen Type		Type I	Type II	Type III
Moment of inertia (cm^4)	I_x	24.51	24.31	24.25
	I_y	1.11	1.80	1.46
(x_c, y_c) (mm, mm)		(12.739; 0)	(23.138; 0)	(33.077; 0)
I_t (cm^4)		25.643	26.11	25.717
I_w (cm^6)		1.058	1.277	9.31
x_0 (cm)		0.713	1.714	2.689
$i_0{}^2$ (cm^2)		8.022	9.498	14.625

Based on $\frac{\partial \Pi}{\partial \xi} = 0$, $\frac{\partial \Pi}{\partial \eta} = 0$, and $\frac{\partial \Pi}{\partial \psi} = 0$, the homogeneous linear equations are obtained as Equations (5)–(7):

$$\xi\left[\left(\frac{n\pi}{L}\right)^2 EI_y - P\right] = 0 \tag{5}$$

$$\eta\left[\left(\frac{n\pi}{L}\right)^2 EI_x - P\right] + \psi P x_0 = 0 \tag{6}$$

$$\eta P x_0 + \psi\left[\left(\frac{n\pi}{L}\right)^2 EI_\omega + GI_t - Pi_0^2\right] = 0 \tag{7}$$

When $n = 1$, the minimum value of P can be obtained. From Equation (5), Equation (8) is obtained.

$$P_1 = P_{cry} = \frac{\pi^2 E I_y}{L^2} \tag{8}$$

where P_{cry} represents the Euler critical force of bending–buckling in the plane of symmetry. The other two roots P_2 and P_3 are calculated by letting $n = 1$ and the coefficient of determination for Equations (6) and (7) being zero is expressed as

$$\begin{vmatrix} \left(\frac{\pi}{L}\right)^2 E I_x - P & P x_0 \\ P x_0 & \left(\frac{\pi}{L}\right)^2 E I_w + G I_t - P i_0^2 \end{vmatrix} = 0 \tag{9}$$

Equation (10) is obtained by expanding the determinant Equation (9).

$$\left(\frac{\pi^2 E I_x}{L^2}\right)^2 \left(\frac{I_\omega}{I_x} + \frac{G I_t L^2}{\pi^2 E I_x}\right) - \frac{\pi^2 E I_x}{L^2}\left(\frac{I_\omega}{I_x} + \frac{G I_t L^2}{\pi^2 E I_x} + i_0^2\right) P + (i_0^2 - x_0^2) P^2 = 0 \tag{10}$$

It is supposed that

$$P_x = \frac{\pi^2 E I_x}{L^2} \tag{11}$$

$$S_1^2 = \frac{I_\omega}{I_x} + \frac{G I_t L^2}{\pi^2 E I_x} \tag{12}$$

By substituting Equation (11) and Equation (12) into Equation (10), Equation (13) can be obtained:

$$s_1^2 P_x^2 - \left(s_1^2 + i_0^2\right) P_x P + \left(i_0^2 - x_0^2\right) P^2 = 0 \tag{13}$$

The two roots P_2 and P_3 can be obtained using Equation (13):

$$P_{2,3} = \frac{P_x}{\frac{s_1^2 + i_0^2}{2 s_1^2} \pm \sqrt{\left(\frac{s_1^2 + i_0^2}{2 s_1^2}\right)^2 - \frac{i_0^2 - x_0^2}{s_1^2}}} \tag{14}$$

The smaller root in Equation (14) is the bending torsional buckling critical load P_{TF}.

$$P_{TF} = \frac{P_x}{\frac{s_1^2 + i_0^2}{2 s_1^2} + \sqrt{\left(\frac{s_1^2 + i_0^2}{2 s_1^2}\right)^2 - \frac{i_0^2 - x_0^2}{s_1^2}}} = \frac{\pi^2 E I_x}{l^2} \cdot \frac{1}{\frac{s_1^2 + i_0^2}{2 s_1^2} + \sqrt{\left(\frac{s_1^2 + i_0^2}{2 s_1^2}\right)^2 - \frac{i_0^2 - x_0^2}{s_1^2}}} \tag{15}$$

When $P_{TF} \geq P_{cry}$, the instability mode of the specimen is bending–buckling. Meanwhile, when $P_{TF} < P_{cry}$, the instability mode is flexural–torsional buckling.

The parameter values of Equation (4) for the experimental specimens were calculated as shown in Table 1. The theoretical values of P_{cry} and P_{TF} for the specimens with different L are all $P_{cry} < P_{TF}$, and the instability mode of the specimens should be bending–buckling. The buckling resistance of the specimens is in the order of Type I > Type II > Type III, which is in the same trend as shown in the experimental results. However, the specimens' instability mode in the theoretical analysis is quite different from that in the experimental results, where flexural–torsional bulking is the instability mode. Therefore, the theoretical value of P_{TF} should be revised to coincide with the experimental results. The correction factors of the experimental specimens Type I–III with different L are shown in Table 2. From Table 2, it is obtained that the average value of the correction coefficient for the experimental specimens Type I–III are 0.0314, 0.0317, and 0.031, i.e., $F_{1\max}^{Ex} = 0.0314 F_{TF}$, $F_{2\max}^{Ex} = 0.0317 F_{TF}$, and $F_{3\max}^{Ex} = 0.031 F_{TF}$, respectively. The mean value of 0.0314, 0.0317, and 0.031 is 0.0314; using this as the correction coefficient for the theoretical analysis, the revised theoretical analysis expression can be obtained as

$$P_{th} = \frac{0.0314\pi^2 EI_x}{l^2} \cdot \frac{1}{\frac{s_1^2+i_0^2}{2s_1^2} + \sqrt{\left(\frac{s_1^2+i_0^2}{2s_1^2}\right)^2 - \frac{i_0^2-x_0^2}{s_1^2}}} \quad (16)$$

Table 2. The experimental and theoretical values for $F_{\max}$.

Specimen Type	Length L (mm)	145	185	220
Type I	Experimental (KN)	24.89	17.91	13
	Theoretical (KN)	859.35	548.42	399.44
	Ratio	0.029	0.0327	0.0325
			The average ratio = 0.0314	
Type II	Experimental (KN)	19.86	16.09	11.79
	Theoretical (KN)	694.36	480.61	357.41
	Ratio	0.029	0.033	0.033
			The average ratio = 0.0317	
Type III	Experimental (KN)	17.89	12.16	9.35
	Theoretical (KN)	532.2	398.89	311.59
	Ratio	0.034	0.03	0.03
			The average ratio = 0.031	

Based on the parameters in Table 1 and Equation (16), the F_{max} values of all specimens tested in the experimental study were calculated and compared with the average value of the experimental data in Figure 5. Generally, the estimated results were close to those of the experimental average values, with a maximum relative error within 10%.

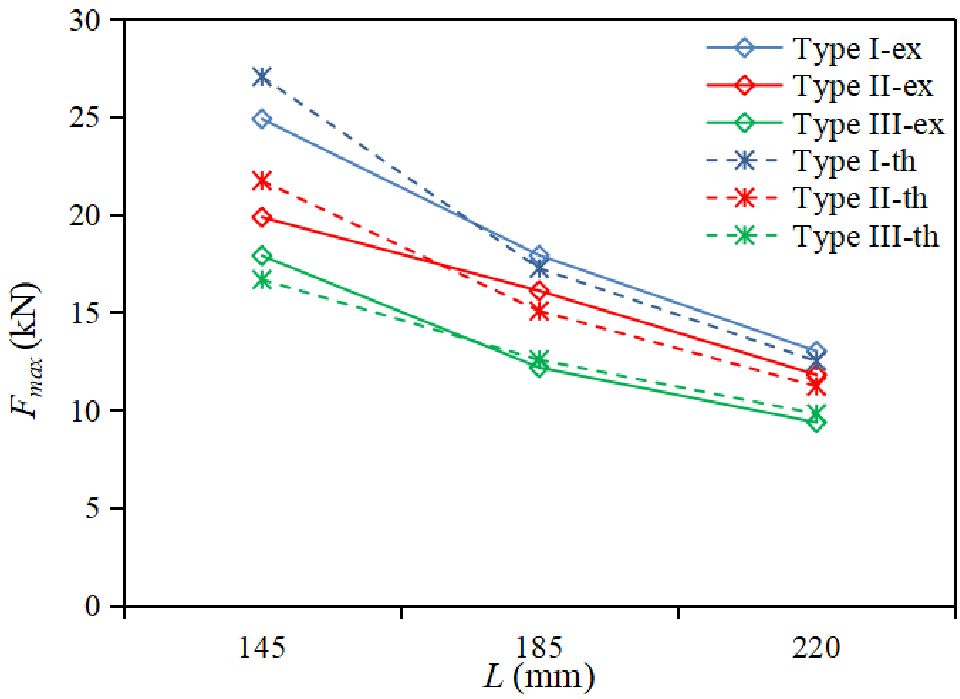

Figure 5. Comparison of theoretical and experimental (average) F_{max} for the specimens with different designs under compression (the abbreviations 'ex' and 'th' represent the experimental and theoretical data, respectively; the lines in blue, red and green represent to cross-section of Type I, Type II and Type III).

4. Discussion

The experimental results (Figure 2a) unsurprisingly indicate the general trend that the maximum force increases with the increasing specimen length under axial compression [25]. However, the maximum displacement of buckling is relatively less sensitive to the increasing specimen length (Figure 2b) compared with the maximum force (Figure 2a). This is largely due to the low toughness of LGFR-PP [10], which limits the failure deformation–length dependency of the specimens under axial compression. It is observed from the experimental results that the cross-section geometry has a significant influence on the buckling resistance of LGFR-PP stiffeners under axial compression; in particular, the buckling resistance of the semicircular cross-sectioned stiffeners is higher than in the designs with rectangular and trapeziform cross-sections, and the trapeziform cross-section has the lowest buckling resistance. This could be explained by the fact that the semicircular cross-section has varying curvature, which is beneficial in reducing the stress concentration [26,27]. In fact, the circular tubes are also found to have a superior specific energy absorption capacity under axial quasi-static crushing than those in other cross-sections, such as triangle, square, pentagon, and hexagon shapes [28]. Regarding the rigidity (lower S_{max}) of the specimens from high to low, it is in the order of Type II ≈ Type III > Type I (Figure 2b), which implies that the rectangular and trapeziform cross-sections are more stable than the semicircular cross-section.

A combination of bending and torsion could be observed in the deformation of the LGFR-PP stiffeners under axial compression (Figure 3), which is similar to that of aramid fiber-reinforced polymer (AFRP) strengthened steel tubes, as found in the literature [25]. This may suggest that the LGFR-PP stiffeners are able to bear a combined load of bending and torsion. The failure behavior of the LGFR-PP stiffeners under axial compression includes matrix cracking, fiber pull-out, or fiber breakage, which is typical for LGFR-PP materials [10,21]. The force–displacement relationship of LGFR-PP stiffeners under axial compression (Figure 3) indicates that the buckling resistance of the LGFR-PP stiffeners mainly relies on elastic and plastic buckling, while the breakage and failure process is relatively sharp given the low toughness of the LGFR-PP material. This finding is similar to those of previous studies of the mechanical properties of fiber-reinforced polymer structures [10,21,25]. The above findings from the experimental study are only based on specimens using LGFR-PP with a glass mass fraction of 40% and randomly oriented fibers; the effects of the glass mass fraction and orientation have not been investigated, but they are important factors affecting the mechanical properties of LGFR-PP structures [4,21,29]. However, a change in these parameters may not affect the basic findings of the current study substantially, given the fact that all the specimens tested here were prepared using the same material and process.

The theoretical study shows that the estimated F_{max} values using the modified elasticity stability theory for a uniform cross-sectioned open thin-walled bar matches the experimental results well (relative error less than 10%) (Figure 5). This implies that the theoretical method demonstrated in the current study is plausible and effective for engineering design, although the "correction coefficient" approach (Table 2 and Equation (16)) is oversimplified. It should be noted that the current study only demonstrates a very basic theoretical approach to estimating the compression resistance capability of LGFR-PP stiffeners, and the influences of the non-linearity of the material being deformed, the formation and growth of micro-cracks, etc., have not been accounted for. Despite much simplification in the theoretical model, there is a relatively fixed ratio (approximately 0.03, Table 2) between the initial theoretical and experimental results, and the demonstrated theoretical method could be used as a preliminary estimation tool for engineering design.

5. Conclusions

The buckling characteristics of different cross-sectioned LGFR-PP stiffeners subjected to axial compression were investigated from experimental tests and theoretical analysis. The experimental results imply that the buckling resistance of the LGFR-PP stiffeners in the semicircular cross-section is higher than those in the designs with rectangular and trapeziform cross-sections, and the trapeziform cross-section has the lowest buckling resistance; the rectangular and trapeziform cross-sectioned stiffeners have better rigidity than those with a semicircular cross-section; the LGFR-PP stiffeners present a flexible–torsional bulking instability mode under axial compression, and the final failure behaviors include matrix cracking, fiber pull-out, and fiber breakage. The theoretical analysis results show that the elasticity stability theory for a uniform cross-sectioned open thin-walled bar modified based on a "correction coefficient" according to the test results could generally estimate the maximum buckling force of LGFR-PP stiffeners under axial compression. The findings of the current work could only provide a basic reference for the design of LGFR-PP stiffeners; the ongoing analysis focusing on the effects of the cross-section design together with the preparation techniques and materials on the mechanical characteristics of LGFR-PP structures under statistic and dynamic compression might provide further detailed information.

Author Contributions: Conceptualization, J.N.; methodology, J.N. and W.G.; writing—original draft preparation, J.N. and W.G.; writing—review and editing, G.L.; funding acquisition, J.N. and G.L. All authors have read and agreed to the published version of the manuscript.

Funding: This study was supported by the Scientific Research Fund of Hunan Provincial Education Department (Grant No. 20B233) and the Natural Science Foundation of Hunan Province (2021JJ60056).

Institutional Review Board Statement: Not applicable.

Informed Consent Statement: Not applicable.

Data Availability Statement: Data is unavailable due to privacy.

Conflicts of Interest: The authors declare no conflict of interest.

References

1. Gao, D.; Zhang, Y.; Wen, F.; Pang, Y.; Fang, D.; Lv, M. Transverse shear properties of fiber reinforced polymer bars with different reinforced phases. *J. Compos. Mater.* **2021**, *55*, 4063–4078. [CrossRef]
2. Bureau, M.N.; Denault, J. Fatigue resistance of continuous glass fiber/polypropylene composites: Consolidation dependence. *Compos. Sci. Technol.* **2004**, *64*, 1785–1794. [CrossRef]
3. Brown, K.A.; Brooks, R.; Warrior, N.A. The static and high strain rate behaviour of a commingled E-glass/polypropylene woven fabric composite. *Compos. Sci. Technol.* **2010**, *70*, 272–283. [CrossRef]
4. Duan, S.; Mo, F.; Yang, X.; Tao, Y.; Wu, D.; Peng, Y. Experimental and numerical investigations of strain rate effects on mechanical properties of LGFRP composite. *Compos. Part B* **2016**, *88*, 101–107. [CrossRef]
5. Friedrich, K.; Hou, M. On stamp forming of curved and flexible geometry components from continuous glass fiber/polypropylene composites. *Compos. Part A* **1998**, *29*, 217–226. [CrossRef]
6. Madra, A.; Hajj, N.E.; Benzeggagh, M. X-ray microtomography applications for quantitative and qualitative analysis of porosity in woven glass fiber reinforced thermoplastic. *Compos. Sci. Technol.* **2014**, *95*, 50–58. [CrossRef]
7. Simeoli, G.; Acierno, D.; Meola, C. The role of interface strength on the low velocity impact behaviour of PP/glass fibre laminates. *Compos. Part B* **2014**, *62*, 88–96. [CrossRef]
8. Trudel-Boucher, D.; Fisa, B.; Denault, J.; Gagnon, P. Experimental investigation of stamp forming of unconsolidated commingled E-glass/polypropylene fabrics. *Compos. Sci. Technol.* **2006**, *66*, 555–570. [CrossRef]
9. Fiorotto, M.; Lucchetta, G. Experimental investigation of a new hybrid molding process to manufacture high-performance composites. *Int. J. Mater. Form.* **2013**, *6*, 179–185. [CrossRef]
10. Mo, F.; Zhang, H.; Yang, X.; Duan, S.; Xiao, Z. Coupling investigation on tensile and acoustic absorption properties of lightweight porous LGF/PP composite. *Polym. Compos.* **2019**, *40*, 1315–1321. [CrossRef]
11. Nassiraei, H.; Rezadoost, P. Static capacity of tubular x-joints reinforced with fiber reinforced polymer subjected to compressive load. *Eng. Struct.* **2021**, *236*, 112041. [CrossRef]
12. Nassiraei, H.; Rezadoost, P. Local joint flexibility of tubular T/Y-joints retrofitted with GFRP under in-plane bending moment. *Mar. Struct.* **2021**, *77*, 102936. [CrossRef]
13. Nassiraei, H.; Rezadoost, P. SCFs in tubular X-connections retrofitted with FRP under in-plane bending load. *Compos. Struct.* **2021**, *274*, 114314. [CrossRef]
14. Ashaab, A.; Rodriguez, K.; Molina, A. Internet-based collaborative design for an injection-moulding system. *Concurr. Eng.* **2003**, *11*, 289–299. [CrossRef]

15. Davoodi, M.M.; Sapuan, S.M.; Yunus, R. Conceptual design of a polymer composite automotive bumper energy absorber. *Mater. Des.* **2008**, *29*, 1447–1452. [CrossRef]
16. Davoodi, M.M.; Sapuan, S.M.; Ali, A.; Ahmad, D. Effect of the strengthened ribs in hybrid toughened kenaf/glass epoxy composite bumper beam. *Life Sci. J.* **2012**, *9*, 285–289.
17. Zhou, Z.; Gan, D.; Zhou, X. Cyclic-shear behavior of square thin-walled concrete-filled steel tubular columns with diagonal ribs. *Eng. Struct.* **2022**, *259*, 114177. [CrossRef]
18. Gan, D.; Zhou, Z.; Zhou, X. Axially loaded thin-walled square concrete-filled steel tubes stiffened with diagonal binding ribs. *ACI Struct. J.* **2019**, *116*, 265–280. [CrossRef]
19. Zhang, Z.; Liu, S.; Tang, Z. Design optimization of cross-sectional configuration of rib-reinforced thin-walled beam. *Thin Walled Struct.* **2009**, *47*, 868–878. [CrossRef]
20. Murata, S.; Shioya, S.; Suffis, B. Expanded polypropylene (EPP): A global solution for pedestrian safety bumper systems. In Proceedings of the SAE 2004 World Congress & Exhibition, Detroit, MI, USA, 8 March 2004.
21. Ephraim, M.; Adetiloye, A. Mechanical properties of glass fibre reinforced polymer based on resin from recycled plastic. *Int. J. Sci. Eng. Res.* **2015**, *6*, 145–152.
22. Sheikh, A.H.; Thomsen, O.T. An efficient beam element for the analysis of laminated composite beams of thin-walled open and closed cross sections. *Compos. Sci. Technol.* **2008**, *68*, 2273–2281. [CrossRef]
23. Wang, S.J. Torsional-flexural buckling of open thin-walled columns with battens. *Thin-Walled Struct.* **1985**, *3*, 323–344. [CrossRef]
24. Zhou, X.H.; Wang, S.J. *Thin-Walled Component Stability Theory and Its Application*; Beijing Science Press: Beijing, China, 2009; pp. 28–33. (In Chinese)
25. Djerrad, A.; Fan, F.; Zhi, X.; Wu, Q. Experimental and FEM analysis of AFRP strengthened short and long steel tube under axial compression. *Thin-Walled Struct.* **2019**, *139*, 9–23. [CrossRef]
26. Liang, C.; Hsu, C.; Chen, W. Curvature effect on stress concentrations around circular hole in opened shallow cylindrical shell under external pressure. *Int. J. Press. Vessel. Pip.* **1998**, *75*, 749–763. [CrossRef]
27. Zakora, S.V.; Chekhov, V.N.; Shnerenko, K.I. Stress concentration around a circular hole in a transversely isotropic spherical shell. *Int. Appl. Mech.* **2004**, *40*, 1391–1397. [CrossRef]
28. Zhu, G.; Sun, G.; Li, G.; Cheng, A.; Li, Q. Modeling for CFRP structures subjected to quasi-static crushing. *Compos. Struct.* **2018**, *184*, 41–55. [CrossRef]
29. Maleki, S.; Tahani, M. Non-linear analysis of fiber-reinforced open conical shell panels considering variation of thickness and fiber orientation under thermo-mechanical loadings. *Compos. Part B* **2013**, *52*, 245–261. [CrossRef]